RSC Advances

PAPER

View Article Online
View Journal | View Issue

Cite this: *RSC Adv.*, 2020, **10**, 42619

Synthesis of $SrTiO_3$ submicron cubes with simultaneous and competitive photocatalytic activity for H_2O splitting and CO_2 reduction†

Haoshan Wei,[ab] Jingyi Cai,[ab] Yong Zhang,*[ab] Xueru Zhang,[c] Elena A. Baranova,[de] Jiewu Cui,[ab] Yan Wang,[ab] Xia Shu,[ab] Yongqiang Qin,[ab] Jiaqin Liu[bf] and Yucheng Wu*[ab]

Single crystalline strontium titanate ($SrTiO_3$) submicron cubes have been synthesized based on a molten salt method. The submicron cubes showed superior photocatalytic activity towards both water splitting and carbon dioxide reduction, in which methane (CH_4) and hydrogen (H_2) were simultaneously produced. The average production rate of methane up to 8 h is 4.39 μmol g^{-1} h^{-1} but drops to 0.46 μmol g^{-1} h^{-1}. However, the average production rate of hydrogen is 14.52 before 8 h but then increases to 120.23 μmol g^{-1} h^{-1} after 8 h. The rate change of the two processes confirms the competition between the H_2O splitting and CO_2 reduction reactions. Band structure and surface characteristics of the $SrTiO_3$ submicron cubes were characterized by diffuse reflective UV-Vis spectroscopy, Mott–Schottky analysis, X-ray photoelectron spectroscopy (XPS) and Fourier transform infrared spectroscopy (FTIR). The results reveal that the simultaneous and competitive production of methane and hydrogen is due to a thermodynamics factor, as well as the competition between the adsorption of carbon dioxide and water molecules on the surface of the faceted $SrTiO_3$. This work demonstrates that $SrTiO_3$ photocatalysts are efficient in producing sustainable fuels *via* water splitting and carbon dioxide reduction reactions.

Received 26th September 2020
Accepted 11th November 2020

DOI: 10.1039/d0ra08246e

rsc.li/rsc-advances

Introduction

Fossil fuel depletion and increased anthropogenic CO_2 emission have been identified as two future challenges triggering global economic and environmental problems.[1,2] Therefore, the development of sustainable energy resources is both essential and urgent. By utilizing the abundant solar energy, it is possible to split H_2O or/and reduce CO_2 using photocatalysts.[3,4] This process produces hydrogen or/and other value-added chemicals from CO_2, as well as simultaneously addressing environmental issues.[5–8]

Perovskite-type oxides are the materials with the general formula ABO_3, in which the larger A cation is coordinated to 12 anions and the B cation occupies 6 coordinated sites forming a network of corner-sharing BO_6 octahedra.[9] The site of A can be larger cations of rare-earth elements – alkaline earth or alkali, whereas the smaller B cations include transition metals.[10] The distortions present in the crystal structure are determined by the ionic radii and valence of cations, which are responsible for the chemical and physical properties of the materials.[10] Due to their broad adaptability, perovskite-type materials have been extensively studied and used for a wide range of applications as catalytic, oxygen transport, ferroelectric, piezoelectric, and dielectric materials.[11–14] Recently, the photocatalytic water splitting and CO_2 reduction properties have been explored in some typical perovskite-type materials.[15–20] For example, $BaTiO_3$ nanoparticles synthesized at room temperature and ambient pressure showed 7 and 1.9 times higher photocatalytic hydrogen evolution than the commercial $BaTiO_3$ in the presence and absence of TEOA as a sacrificial agent, respectively.[21] Beata's group reported that silver deposited on the surface of $LiNbO_3$ in the form of Ag_2O was responsible for the enhanced photocatalytic activity in the studied reaction.[22] Balasubramanian *et al.* reported photocatalytic reduction of CO_2 by water under UV-visible light over La modified $NaTaO_3$, which showed a stable performance for up to 20 hours.[23]

[a]*School of Materials Science and Engineering, Hefei University of Technology, Hefei 230009, Anhui, China. E-mail: zhangyong.mse@hfut.edu.cn; ycwu@hfut.edu.cn*
[b]*Key Laboratory of Advanced Functional Materials and Devices of Anhui Province, Hefei 230009, Anhui, China*
[c]*Instrumental Analysis Center, Hefei University of Technology, Hefei 230009, China*
[d]*China International S&T Cooperation Base for Advanced Energy and Environmental Materials, Hefei 230009, Anhui, China*
[e]*Department of Chemical and Biological Engineering, Centre for Catalysis Research and Innovation (CCRI), University of Ottawa, 161 Louis-Pasteur, Ottawa, ON K1N 6N5, Canada*
[f]*Institute of Industry & Equipment Technology, Hefei University of Technology, Hefei 230009, Anhui, China*

† Electronic supplementary information (ESI) available. See DOI: 10.1039/d0ra08246e

$SrTiO_3$ has a theoretical band gap width of 3.24 eV (ref. 24 and 25) in which both the conduction and the valence band potential satisfy the thermodynamic conditions of photocatalytic water splitting and photocatalytic reduction of carbon dioxide.[26] This makes $SrTiO_3$ a good candidate for various photocatalytic processes.[27,28] However, the pure $SrTiO_3$ suffers from a low utilization of visible light, because it only responds in the ultraviolet region, difficulty in recovery, complex preparation methodology and low photocatalytic activity due to the easy recombination of photogenerated electrons and holes.[29]

Many efforts have been done to improve chemical and physical properties of $SrTiO_3$ by altering its composition through additional oxygen vacancies and element doping.[30–32] For example, Ye *et al.* prepared a Ti^{3+} self-doped $SrTiO_{3-\delta}$ photocatalyst with enhanced activity for artificial photosynthesis under visible light by oxygen vacancy accommodated in perovskite.[33] Another work investigated the influence of N, S and Fe doping on photocatalytic CO_2 reduction performance of strontium titanates.[34] Up to date, there are very few reports that investigate the simultaneous water splitting and CO_2 reduction and their competitive nature over $SrTiO_3$ nano- or submicron cubes. It is known that pure CH_4 has characteristics of low flame propagation speed, small flammable limit range, and low thermal efficiency, resulting in low combustion efficiency and large fuel consumption. However, the mixture gas of H_2 to CH_4 has the advantages of increasing the flammability limit, speeding up the spread of flames, and reducing the emission of pollutants.[35] The simultaneous CO_2 conversion and water splitting through photocatalysts can provide a simple and energy-saving method for obtaining the mixed gas of CH_4 and H_2. Moreover, the selectivity of photocatalysts to produce mixed gas with different mixing ratios deserves more attention which is of great significance for unveiling the origin of catalytic selectivity as well as finding great potential applications. The unveiling the origin of the crystal facets of the nano- or submicron on the catalyst performance is a key question for the efficient synthesis of useful chemicals.

In this work, we report the preparation of perovskite strontium titanate submicron cubes photocatalysts by the molten salt synthesis method, which is one of the attractive techniques with merits of one-step, facile, time-saving, and versatile.[36] Photocatalysis measurements suggest that methane and hydrogen are simultaneously and competitively produced on the $SrTiO_3$ submicron cubes surface during photocatalytic reduction of carbon dioxide with water. The competitive relationship between the two reactions is investigated and the reaction mechanism is proposed.

Experimental

Chemicals and materials

$SrCO_3$ (AR, 99.8%), $H_2PtCl_6 \cdot 6H_2O$ (AR, Pt 37.5%), triethanolamine and ethanol (AR, 99.5%) were purchased from Sinopharm Chemical Reagent Company. P25 TiO_2 (AR, 99.8%), NaCl (AR, 99.5%) and KCl (AR, 99.5%) were purchased from Aladdin Reagent Company. All chemicals were used as received without any further purification.

Synthesis of $SrTiO_3$ submicron cubes

$SrTiO_3$ submicron cubes were prepared by the molten salt synthesis method as reported previously.[37] In the typical synthesis of $SrTiO_3$ submicron cubes, $SrCO_3$, TiO_2, NaCl and KCl were mixed in an overall stoichiometric ratio of 1 : 1 : 50 : 50. Then the mixture was put into the mortar and grinded thoroughly for 30 min. Next, the mixture was put into an alumina crucible and then heated to 700 °C at a rate of 5 °C min^{-1} in a muffle furnace and maintained at this temperature for 5 h. After cooling down to room temperature, the sample was washed with deionized water (18.25 MΩ cm) several times to remove NaCl and KCl. Then washed with diluted hydrochloric acid (0.05 M) to remove unreacted impurity of $SrCO_3$. Finally, dried in an oven at 60 °C for 12 h.

Preparation of Pt nanoparticles loaded $SrTiO_3$ submicron cubes

Pt nanoparticles loaded $SrTiO_3$ submicron cubes were prepared in a traditional method of photodeposition.[38] In a typical experiment, 100 mg as-prepared $SrTiO_3$ submicron cubes sample was dispersed in 100 mL of deionized water containing 20 mL of triethanolamine (TEOA) by sonication for 10 min. The prepared solution H_2PtCl_6 (20 mmol L^{-1}) were added into the above dispersion solution with the mass ratio of Pt/$SrTiO_3$ 3%. The solution was then sealed and evacuated with a vacuum pump to remove oxygen from the solution and stirred in dark for $SrTiO_3$ submicron cubes fully adsorbing metal ions. After 30 min, the solution was irradiated from the top by a 300 W Xe lamp (PLS-SXE 300, Beijing Trusttech Co. Ltd, China) with simulated sunlight for 4 h. The sample was collected by centrifugation and washed with deionized water and ethanol. Then, dried in a vacuum drying oven oven at 60 °C for 12 h. The as-obtained samples were marked as STO-Pt.

Physicochemical characterization

The X-ray diffraction (XRD, $2\theta = 3°$ min^{-1}, 2 h = 10–90°, D/MAX2500V, Rigaku Corporation, Japan) analyses were performed to characterize the crystal structure. The microstructure of the $SrTiO_3$ nanocrystal was investigated by scanning electron microscopy (SEM, SU8020, HITACHI, Ltd., Japan). The valence states of the elements in the $SrTiO_3$ nanocrystals were analyzed using an ESCALAB250 spectrometer equipped with an Al Ka (1486.6 eV) radiation source. Transmission electron microscopy (TEM) analysis with selected-area diffraction was carried out on a JEOL 2100F field-emission transmission electron microscope operated at 200 kV. The UV-Vis absorption spectra were recorded on a UV-3600 UV-Vis-NIR scanning spectrophotometer (Shimadzu).

Photocatalytic activity measurements

50 mg of photocatalyst STO-Pt was placed into an aqueous triethanolamine (TEOA) solution (100 mL, 10 vol%) in a closed gas circulation system (Perfect Light Company Labsolar-III (AG)). The CO_2 (99.99%) gas flow rate into the reactor was controlled at 10 mL min^{-1} for 45 min using a mass flow

controller (D08-3F, Sevenstar, China). UV-Vis light and visible light irradiation were obtained from a 300 W Xe lamp (PLS-SXE 300, Beijing Trusttech Co. Ltd, China) with Simulated sunlight. The evolved gases were detected *in situ* using an online gas chromatograph (GC-7890B, Agilent) equipped with a thermal conductivity detector (TCD) and flame ionization detector (FID). In addition, a control experiment of water splitting was carried out under the same conditions but in the absence of carbon dioxide.

Mott–Schottky measurements

$SrTiO_3$ thin film photoelectrodes were prepared by electrophoretic deposition on the FTO substrate as reported previously.[39] In a typical process, FTO glasses (3 cm × 1 cm × 0.22 cm) were ultrasonically cleaned sequentially with acetone, ethanol and water for 30 minutes each. Electrophoretic deposition was carried out in 70 mL acetone solution containing 30 mg iodine. The FTO electrode, with 1 cm^2 deposition area immersed into the solution, was parallel to the Pt electrode. The distance between two electrodes was 80 mm. A 40 V bias was applied for 3 min between two electrodes using a potentiostat (ITECH IT6834). The deposited $SrTiO_3$ electrodes were dried in the air at room temperature and subjected to calcination at 350 °C for 30 min. Mott–Schottky experiments were carried out in a three-electrode electrochemical setup in 0.5 mol L^{-1} Na_2SO_4 electrolyte. The deposited $SrTiO_3$ electrode, the platinum electrode and silver/silver chloride electrode (Ag/AgCl) were used as a working, counter and reference electrode, respectively.

Results and discussion

The crystallite structure of the as-prepared sample was characterized by X-ray diffraction. Fig. 1 shows strong peaks are very similar to purchased $SrTiO_3$ commercial powders, which correspond to cubic $SrTiO_3$ phase (JCPDS no. 86-0179) with space group $Pm\bar{3}m$ (221). No additional diffraction peaks are observed, suggesting the high purity of the obtained $SrTiO_3$ crystals. Fig. S1† presents the XRD Rietveld refinement patterns of the $SrTiO_3$ crystal. The refinement of the sample yields χ^2, wR_p and R_p values of 1.817, 6.54% and 5.8%, respectively, indicating close agreements with the experimental data. The crystal cell parameter of the prepared $SrTiO_3$ is 3.10931 (15) Å, and the unit cell volume is 59.379 (7) $Å^3$. Based on the experimental and calculated results, it was confirmed that the synthesized sample has a perovskite structure.

The morphology of the $SrTiO_3$ sample was observed by the scanning electron microscopy (SEM). Fig. 2(a) and (b) show that as-synthesized $SrTiO_3$ sample has a cubic shape. Fig. 2(c) and (d) shows the particle size distribution and high resolution TEM images of $SrTiO_3$, respectively. TEM images reveal that the side average length of the cubes is about 79 nm, which have been shown in Fig. S2.† The grain size calculated by the Scherrer's formula, $D = K\gamma/B\cos\theta$, is 83 nm. These two values are very similar. So, it is proved that the prepared cubes have single crystal nature with a clear lattice fringe spacing of 0.28 nm in the direction of (110) and (1$\bar{1}$0) and a lattice fringe spacing of 0.19 nm for (200) and (020). In addition, HRTEM characterization shown in Fig. 2(d) suggests the faceted shape of the cubic particle, which is enclosed with (200) planes at the edge and planes at the corner. The single crystal nature of $SrTiO_3$ cubes can be confirmed by the selected area electron diffraction (SAED) pattern as shown in Fig. 2(e). Furthermore, Fig. 2(f)–(h) show TEM and HRTEM images of the $SrTiO_3$ submicron cubes loaded with Pt nanoparticles of 2–4 nm in size.

X-ray photoelectron spectroscopy (XPS) was used to characterize the elemental surface composition of the photocatalyst. All XPS spectra were fitted using a Shirley-type background subtraction method. The background functions were fitted using 80% Gaussian and 20% Lorentzian functions.[40] Fig. 3(a) shows that titanium is present in the Ti^{4+} state in the $SrTiO_3$ sample, which is fitted out using two peaks at 458.2 and 463.9 eV, corresponding to Ti^{4+} $2p_{3/2}$ and Ti^{4+} $2p_{1/2}$, respectively. However, the XPS peaks of titanium in the Pt loaded $SrTiO_3$ sample are shifted positively to 458.51 and 464.26 eV (Fig. 3(a)). This shows that part of the electrons on the Ti element are

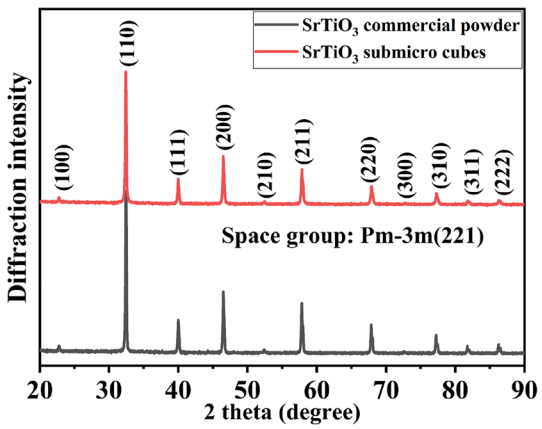

Fig. 1 XRD pattern of the as-prepared $SrTiO_3$ synthesized by molten salt method.

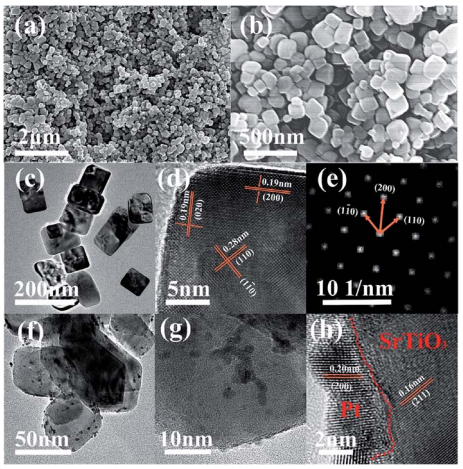

Fig. 2 (a and b) SEM of $SrTiO_3$, (c) low resolution TEM of $SrTiO_3$, (d) high resolution TEM of $SrTiO_3$ lattice fringes, (e) selected area electron diffraction pattern of $SrTiO_3$, (f, g) TEM of STO-Pt, (h) high resolution TEM of STO-Pt lattice fringes.

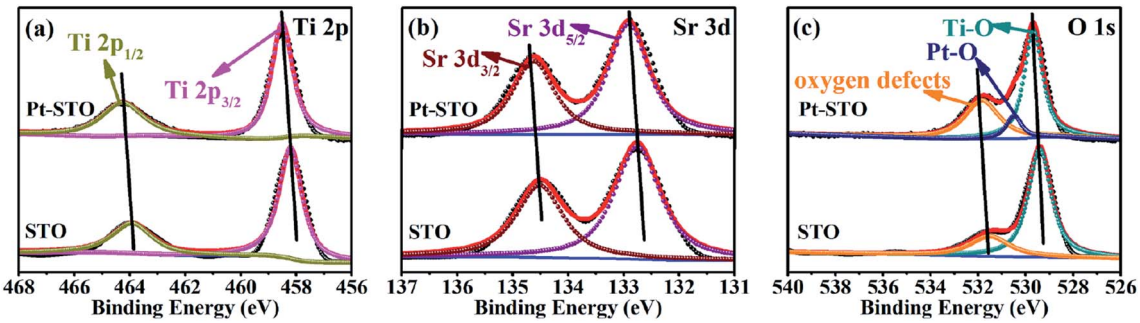

Fig. 3 High resolution XPS spectra of (a) Sr 3d, (b) Ti 2p, (c) O 1s in $SrTiO_3$ sample.

transferred onto the surface of the Pt nanoparticles in the Pt loaded photocatalyst. This peak shift also occurs for Sr and O elements. The Sr^{2+} $3d_{5/2}$ and $3d_{3/2}$ peaks, shown in Fig. 3(b) are observed at 132.75 and 134.51 eV, respectively and are shifted to 132.92 and 134.63 eV in the presence of Pt. High resolution XPS spectrum of O 1s in Fig. 3(c) illustrates two peaks at 529.4 and 531.5 eV. The peak at 529.4 eV is associated with the lattice O^{2-} ions in the crystal structure. And the peak at 531.4 eV is attributed to O^{2-} in the oxygen defects –OH at cubic $SrTiO_3$ surface, which may be beneficial for photocatalytic water splitting and photocatalytic reduction of carbon dioxide.[41,42] The two peaks are also shifted positively to 529.66 and 531.83 eV, respectively for Pt loaded sample. Notably, the significant increase of the peak attributing to O^{2-} in the oxygen defects –OH indicate the more absorption site for H_2O, which is conducive to the photocatalytic reaction. The peak at 530.48 eV corresponds to Pt–O. Fig. S3† shows the higher resolution XPS spectra of Pt. It can be seen that platinum has three valence states, which is fitted using six peaks at 70.8 and 74.42 eV corresponding to Pt^0, 71.34 and 75.98 eV corresponding to Pt^{2+} and 72.27 and 78.08 eV corresponding to Pt^{4+}, respectively. The appearance of high-valence Pt may be due to oxidation of part of Pt during photodeposition by the high activity holes. It confirmed that the Schottky junction is formed at the interface between $SrTiO_3$ and Pt nanoparticles.[43] The Tauc plot of $SrTiO_3$ samples is shown in Fig. S4.† The optical bandgap of $SrTiO_3$ is about 3.23 eV.

Photocatalytic activity of the $SrTiO_3$ submicron cubes was investigated for CO_2 reduction and water splitting. Our experimental results indicate that the submicron cubes show superior activity for a simultaneous production of CH_4 and H_2. Fig. 4 shows the production rate of CH_4 and H_2 over $SrTiO_3$ loaded with 3 wt% Pt under UV-Vis light (300 W Xe lamp) using 20 vol% triethanolamine (TEOA) as sacrificial agent. From the plots, it can be seen that the $SrTiO_3$ submicron cubes exhibit superior activity towards both CO_2 reduction and water splitting. As known, crystal facets play a crucial role in photocatalysis due to their different surface energy. As discussed in the HRTEM and SAED characterization section (Fig. 2), the obtained $SrTiO_3$ submicron cubes are enclosed with (100) plane at the edge and (110) plane at the corner of the $SrTiO_3$ cubes. The $SrTiO_3$ (100) surface is the most thermodynamically stable facet, which can be terminated by a SrO or TiO_2 plane with a similar surface energy of 6.85 eV nm^{-2}.[44–46] For the (110) facet, there are two alternating layers of $SrTiO^{4+}$ and $O_2{}^{4-}$, forming an unbalanced dipole with a high surface energy of 20.02 eV nm^{-2}.[46,47] The terminal plane of the two facets is shown in Fig. S5.† Directional separation of photogenerated electron–hole pairs is due to differences in surface energy, which is conducive to the separation of photogenerated carriers[48–50] thereby enhancing the photocatalytic activity of the submicron cubes for the CO_2 reduction and water splitting.

Quantitively analysis on the photocatalytic activity of the submicron cubes indicated that for the CO_2 reduction, the

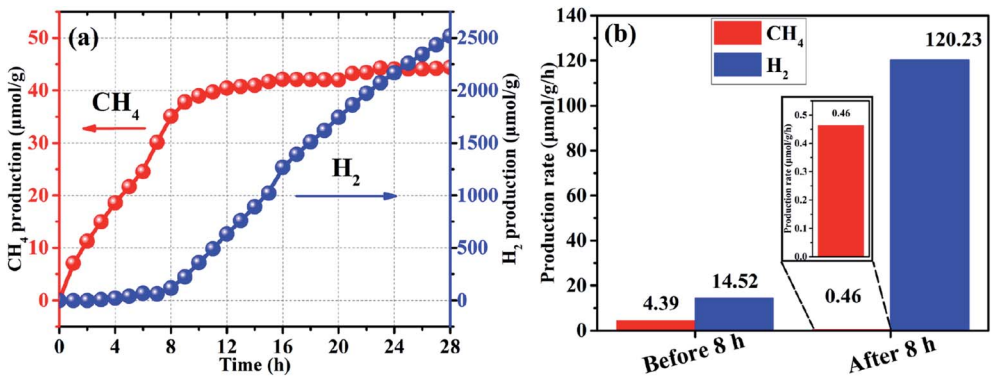

Fig. 4 (a) Photocatalytic reduction of CO_2 over STO-Pt with under simulated sunlight with 20% volume ratio of triethanolamine (TEOA) as sacrificial agent, (b) production rate change before and after eighth hour.

production of CH_4 increases rapidly with an average production rate of 4.39 μmol g^{-1} h^{-1} at the first 8 h as shown in Fig. 4(b), then the CH_4 amount tends to reach a plateau with the average CH_4 production rate down to 0.46 μmol g^{-1} h^{-1} when $8 \leq t \leq 28$ h. On the other hand, the rate of H_2 production by photocatalytic water splitting increases gradually at the first 8 h with an average rate of 14.52 μmol g^{-1} h^{-1}, then the H_2 production rate increases rapidly to 120.23 μmol g^{-1} h^{-1} from the 8th to the 28th hrs. Interestingly, a negative correlation between the production of CH_4 and H_2 can be observed in Fig. 4(a), demonstrating a clear competitive relationship between the two reactions. In addition, the competitive correlation is altered with the reaction time. From the results of the third repetitive test of photocatalytic reduction of CO_2 on the same sample (Fig. S6†), it can be obviously seen that the law of the production of CH_4 and H_2 is almost the same as the results in the first round test. Therefore, it can be inferred that the surface chemistry evolution during the photocatalytic reaction is recoverable. Nevertheless, there is a certain attenuation of the production rates of CH_4 and H_2, which may be caused by possible property fading of the catalysts after the long-time reaction. Some references have been listed for comparison with our experiments in the ESI† (Table S1†). Based on the information in the table, it can be seen that the material we prepared has a good performance of photocatalytic reduction of carbon dioxide with simultaneous photocatalytic water splitting, demonstrating that our method is a rational strategy to design Ti-based photocatalysts for photocatalytic reduction of CO_2.

To determine whether the generated CH_4 and H_2 come from the photocatalytic decomposition of the scarifying reagent of triethanolamine in water, two comparative experiments have been implemented. First one is to control for all other conditions the same except for the absence of carbon dioxide. The results are shown in the Fig. S7.† The H_2 production rate is 426.41 μmol g^{-1} h^{-1}, but no methane is produced. The other one was performed in pure phase triethanolamine with all other conditions the same, but no gaseous products were detected. Based on the above results, it suggests that the generated CH_4 and H_2 are not supposed to come from the photocatalytic decomposition of the scarifying reagent of triethanolamine in water.

To get insight into the correlation between the CH_4 and H_2 production, the band structure characteristics of the obtained $SrTiO_3$ submicron cubes were investigated by the Mott–Schottky measurement. This approach is as a powerful and widely used tool to determine capacitance, carrier density and flat band potential.[51] The presented $1/C^2$ obtained from impedance spectroscopy at three frequencies, 1000, 2000 and 5000 Hz, shown in Fig. 5. The flat-band potential of the semiconductor could be extracted from the *x*-axis intersection. As illustrated in Fig. 5(a), the flat band potential of the prepared $SrTiO_3$ sample measured at three different frequencies is almost identical at approximately −0.14 *vs.* RHE, which is in agreement with the reported values.[52–54] Combined with the measured band gap value (Fig. S4†), the band structure of prepared $SrTiO_3$ sample has been obtained in Fig. 5(b). A proper equivalent circuit (Fig. S8†) has been used to fit the EIS plots for further understanding the conductivity of the photocatalysts. R_{ct} can be assigned to the charge-transfer resistance in the photocatalyst. The charge-transfer resistances for $SrTiO_3$ submicro cubes is 104 590 Ω, which is smaller than that of $SrTiO_3$ commercial powder, 118 170 Ω. This proves the more effective separation and transportation of photo-generated carriers in $SrTiO_3$ submicro cubes. As we all know, the thermodynamic condition of the photocatalytic reduction reaction is that the conduction band edge of the semiconductor is higher than the standard reduction potential of the reactant, and the photocatalytic oxidation reaction occurs only when the valence band edge of the semiconductor is lower than the standard oxidation potential of the reactant. As shown in Fig. 5(b), the potential of H^+/H_2 (0 V *vs.* NHE at pH 7) for the redox reaction is more negative than that of CO_2/CH_4 (0.21 V *vs.* NHE at pH 7), resulting in easier production of methane than hydrogen.[7] Therefore, from the perspective of thermodynamics, the photo-reduction of CO_2 to CH_4 is more likely to occur than H_2O to H_2.

To confirm the reason for the selectivity changes, $SrTiO_3$ with different Pt loadings were used to test the performance of photocatalytic reduction of CO_2. When no Pt NPs are loaded, the signal of CH_4 and H_2 cannot be detected in the gas chromatography. This is due to the characteristics of $SrTiO_3$ that can only respond in the ultraviolet region and the high recombination efficiency of photogenerated carriers. So, the samples

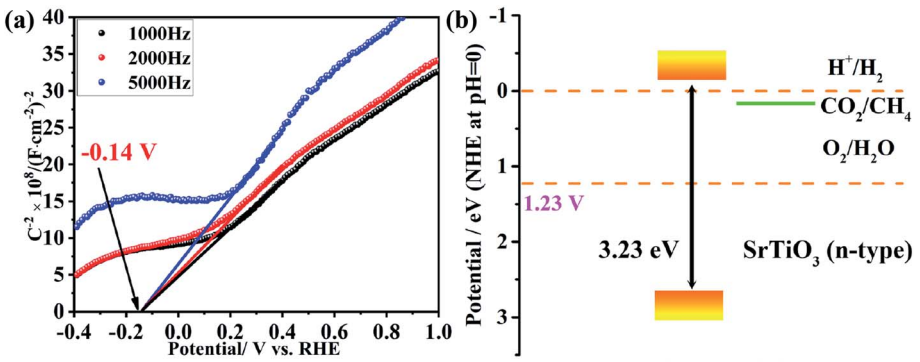

Fig. 5 Band structure of $SrTiO_3$ nanocrystals. (a) The Mott–Schottky curves of $SrTiO_3$ electrodes measured in Na_2SO_4 solution. (b) The scheme of the band structure of $SrTiO_3$ nanocrystals.

with 1 wt% and 5 wt% Pt loaded were used for the photocatalytic CO_2 reduction test (Fig. 6). No obvious inflection point was found for the amount of hydrogen generated in the sample loaded 1 wt%. However, the pattern similar to the sample with 3 wt% Pt loaded has been found for the sample 5 wt% Pt loaded. Therefore, this selectivity change may be closely related to Pt. The production rate of CH_4 and H_2 have an obvious dependence on the load amount of Pt. The production rate of CH_4 is arranged in order as 3 wt% Pt > 1 wt% Pt > 5 wt% Pt; for H_2 is 3 wt% Pt > 5 wt% Pt > 1 wt% Pt. During the reactions, the appropriate Pt NPs loading can improve the separation efficiency of photogenerated electron–hole pairs and act as a catalytic site for water splitting. When the loading amount of Pt NPs is low, the water splitting efficiency and carrier separation are relatively low. However, when the loading amount is too large, Pt NPs will increase the recombination efficiency of carriers, which is not conducive to the progress of the photocatalytic reaction. And also reduce the utilization efficiency of the Pt. Additionally, the photocatalytic reduction of CO_2 performance over STO-Pt under simulated sunlight with 10% and 100% volume ratio of TEOA as sacrificial agent have been tested. The results tested in 10% volume ratio of TEOA has been obtained in Fig. S9,† which are similar to the performance tested in the reaction solution containing 20% volume ratio of TEOA. No gas is generated in the system of 100% volume ratio of TEOA. These results demonstrate that the selectivity changes are not necessarily related to TEOA.

As is known, when the Pt NPs are loaded onto the $SrTiO_3$, the surface electron density of $SrTiO_3$ increases because of the lower Fermi energy of Pt NPs and the surface nanojunctions of Pt-$SrTiO_3$ are formed. After Pt NPs were loaded, the photocatalytic performance was significantly improved, as shown in Fig. 4 and 6. The formed nanojunctions at the interface of Pt NPs and $SrTiO_3$ maybe a crucial factor in performance improvement. For the water splitting reaction, Pt itself is a good hydrogenation and dehydrogenation catalyst, and it has good adsorption and desorption of hydrogen. It is reasonable to deduce that the reaction sites of water splitting are mainly on the surface of Pt NPs. However, the sites of CO_2 reduction on Pt loaded materials are not clear because of the divergent research conclusions that have been reported.[55–58] It should be noted that both hydrogen generation and methane production occurred simultaneously in our experiments, however, it looks that the evolution of methane suppressed the production of hydrogen. While the evolution of methane declined, production of hydrogen was obviously enhanced. The reaction process may be as follows: in the early stage of the reaction, the concentration of CO_2 molecules adsorbed on the surface of $SrTiO_3$ was sufficiently high, which is the main reason for the high rate of CH_4 generation during this period; however, as the reaction proceeded, surface chemistry or microstructure of the adsorption site of CO_2 might change, making it more inclined to promote the hydrogen production. This can be confirmed by the repetitive experiments results (Fig. S6†) and subsequent X-ray photoelectron spectroscopy tests (Fig. 7). That is the reason why the competitive mechanism between the two reactions was proposed.

To confirm our assumption, changes of the surface chemistry and the electronic structure of the samples *vs.* reaction time were determined by XPS as shown in Fig. 7. In this figure, STO-Pt-2h and STO-Pt-15h correspond to the samples of STO-Pt after 2 h and 15 h reaction, respectively. The XPS peaks of Ti in STO-Pt-15h are negatively shifted from 458.51 and 464.26 eV, to 458.21 and 463.9 eV, respectively (Fig. 7(a)). This peak shift also occurs for the Sr and O. The Sr^{2+} $3d_{5/2}$ and $3d_{3/2}$ peaks, shown in Fig. 7(b) are shifted to 134.4 and 132.67 eV, respectively. High resolution XPS spectrum of O 1s, illustrated in Fig. 7(c), indicates that the lattice O^{2-} ions in the crystal structure shifted to 529.34 eV from 529.66 eV, which implies breakdown of the Schottky junction. And the peak attributed to O^{2-} in the oxygen defects –OH on the cubic $SrTiO_3$ surface becomes stronger with the reaction time, indicating that the adsorption of H_2O for the sample of STO-Pt-15h is easier than the sample of STO-Pt-2h.

FTIR was carried out to measure the vibration mode of the bonds in the as-prepared STO, STO-Pt-2h and STO-Pt-15h. As shown in Fig. 7(d), the absorption peak at 1637 cm^{-1} originates from hydroxyl vibration. It is speculated that the hydroxyl group (H–O–H bending) was derived from the adsorption water on the surface of the sample. The transmission peaks at 1475 cm^{-1} probably corresponds to C=O stretching (mode in Sr-OOC). The broad absorption band at 760 to 557 cm^{-1} and the absorption peak at 856 cm^{-1} belong to the characteristic stretching vibration of the Ti–O bond (stretching vibration) and

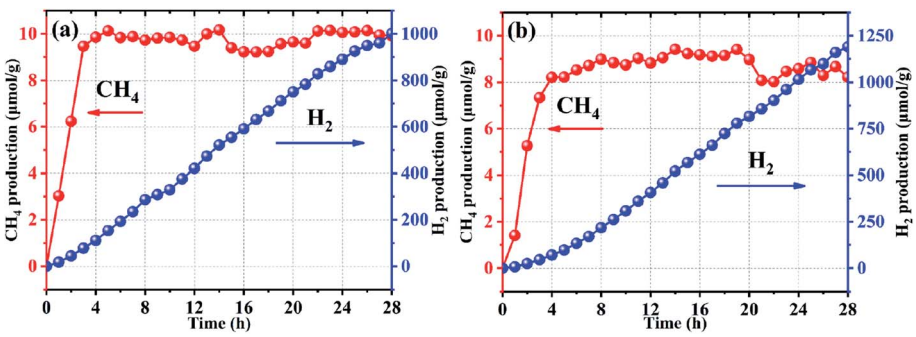

Fig. 6 (a) Photocatalytic reduction of CO_2 over $SrTiO_3$ loaded with 1 wt% Pt under simulated sunlight with 20% volume ratio of triethanolamine (TEOA) as sacrificial agent, (b) photocatalytic reduction of CO_2 over $SrTiO_3$ loaded with 5 wt% Pt under simulated sunlight with 20% volume ratio of triethanolamine (TEOA) as sacrificial agent.

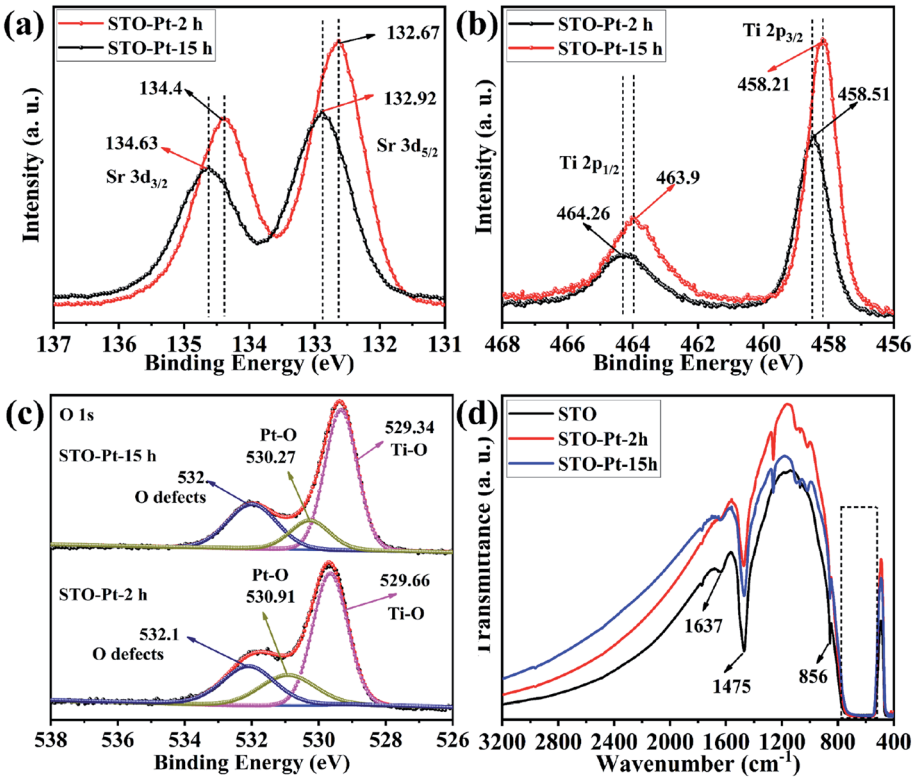

Fig. 7 High resolution XPS spectra of (a) Sr 3d, (b) Ti 2p, (c) O 1s in STO-Pt-2h and STO-Pt-15h samples. (d) FTIR absorption spectra of $SrTiO_3$, STO-Pt-2h and STO-Pt-15h.

Sr–O/Ti–O (octahedron bending), respectively. The absorption peak of Ti–O bond is widened probably due to the presence of several Sr–Ti–O absorption peak.[59] Notably, the absorption peak derived from the adsorption of water on the surface is apparently stronger for the sample STO-Pt-15h than STO-Pt-2h, which also confirms the assumption that adsorption of water onto the surface of $SrTiO_3$ submicron cubes is favored over CO_2 adsorption as the reaction proceed at the surface chemical modification of the photocatalyst take place with time.

Conclusion

In this work, $SrTiO_3$ submicron cubes were successfully prepared by a molten salt synthesis method. A simultaneous and competitive photocatalytic generation of CH_4 and H_2 were observed on the submicron cubes originated from the reduction of CO_2 and water splitting. The generation of CH_4 is higher in the first 8 h with the average production rate of 4.39 μmol g^{-1} h^{-1}, then gradually reaches a plateau area between 8 and 28 hours with the average production rate of 0.46 μmol g^{-1} h^{-1}. On the contrary, evolution of H_2 is evidently suppressed in the first 8 h and increases significantly between 8 to 28 hours, with the average production rate increase from 14.52 μmol g^{-1} h to 120.23 μmol g^{-1} h^{-1}. The investigated surface chemistry and electronic structure of $SrTiO_3$ submicron cubes, photoreduction reaction thermodynamic conditions and competing relationship of reactant molecular adsorption on the surface of $SrTiO_3$ are proposed as the main causes of product rate changes. The current work expands our understanding of the application of photocatalyst for photocatalytic reduction of carbon dioxide and water.

Conflicts of interest

There are no conflicts to declare.

Statement of contributions

Haoshan Wei: Writing-Original Draft, Methodology, Investigation. Jingyi Cai: Methodology, Investigation. Yong Zhang: Resources, Investigation, Supervision, Writing-Reviewing and Editing. Xueru Zhang: Methodology, Investigation. Elena A. Baranova: Writing-Reviewing, Software. Jiewu Cui: Validation, Investigation. Yan Wang: Validation, Software. Xia Shu: Methodology, Investigation Yongqiang Qin: Investigation. Jiaqin Liu: Investigation, Supervision. Yucheng Wu: Resources, Project administration, Editing.

Acknowledgements

This project is supported by Key Project of Changfeng-HFUT Industrial Innovation Guidance Funds (JZ2020YDZJ0122), the National Natural Science Foundation of China (Grant No. 51772072, 51672065, U1810204), Fundamental Research Funds for the Central Universities (PA2019GDQT002, PA2019GDZC0096). We also would like to thank the financial

support from the 111 Project "New Materials and Technology for Clean Energy" (B18018).

References

1 M. Mikkelsen, M. Jørgensen and F. C. Krebs, *Energy Environ. Sci.*, 2010, **3**, 43–81.
2 A. Goeppert, M. Czaun, J. P. Jones, G. K. S. Prakash and G. A. Olah, *Chem. Soc. Rev.*, 2014, **43**, 7995–8048.
3 M. Marszewski, S. Cao, J. Yu and M. Jaroniec, *Mater. Horiz.*, 2015, **2**, 261–278.
4 C. Dong, M. Xing and J. Zhang, *Mater. Horiz.*, 2016, **3**, 608–612.
5 S. Xie, Q. Zhang, G. Liu and Y. Wang, *Chem. Commun.*, 2015, **52**, 35–59.
6 N. S. Lewis and D. G. Nocera, *Proc. Natl. Acad. Sci. U. S. A.*, 2006, **103**, 15729–15735.
7 X. Chang, T. Wang and J. Gong, *Energy Environ. Sci.*, 2016, **9**, 2177–2196.
8 N. U. Stefan, M. A. Juan Antonio and G. Hermenegildo, *Int. J. Mol. Sci.*, 2014, **15**, 5246–5262.
9 K. Karuppiah and A. M. Ashok, *Nanomater. Nanotechnol.*, 2019, **8**, 51–58.
10 A. R. West, *Chem. Rec.*, 2006, **6**, 206–216.
11 C. D. Chandler, C. Roger and M. J. Hampden-Smith, *Chem. Rev.*, 1993, **93**, 1205–1241.
12 A. Bhalla, R. Guo and R. Roy, *Mater. Res. Innovations*, 2000, **4**, 3–26.
13 M. Pena and J. Fierro, *Chem. Rev.*, 2001, **101**, 1981–2018.
14 F. Kyoichi, K. Kiyofumi, K. Jumpei, H. Tadashi and K. Kunihito, *Nanoscale*, 2010, **2**, 2080–2083.
15 M. Zhou, J. Chen, Y. Zhang, M. Jiang, S. Xu, Q. Liang and Z. Li, *J. Alloys Compd.*, 2020, **817**, 152796.
16 E. Can and R. Yildirim, *Appl. Catal., B*, 2019, **242**, 267–283.
17 R. Shi, G. I. N. Waterhouse and T. Zhang, *Sol. RRL*, 2017, **1**, 1700126.
18 K. M. Macounová, R. Nebel, M. Klusáčková, M. Klementová and P. Krtil, *ACS Appl. Mater. Interfaces*, 2019, **11**, 16506–16516.
19 A. Alzahrani, D. Barbash and A. Samokhvalov, *J. Phys. Chem. C*, 2016, **120**, 19970–19979.
20 F. Yang, Q. Zhang, L. Zhang, M. Cao, Q. Liu and W.-L. Dai, *Appl. Catal., B*, 2019, 117901.
21 T. Chen, J. Meng, S. Wu, J. Pei, Q. Lin, X. Wei, J. Li and Z. Zhang, *J. Alloys Compd.*, 2018, **754**, 184–189.
22 B. Zielińska, *Bull. Mater. Sci.*, 2014, **37**, 911–916.
23 V. Jeyalakshmi, S. Tamilmani, R. Mahalakshmy, P. Bhyrappa, K. R. Krishnamurthy and B. Viswanathan, *J. Mol. Catal. A: Chem.*, 2016, **420**, 200–207.
24 C. E. Ekuma, M. Jarrell, J. Moreno and D. Bagayoko, *AIP Adv.*, 2012, **2**, 129.
25 S. Piskunov, E. Heifets, R. Eglitis and G. Borstel, *Comput. Mater. Sci.*, 2004, **29**, 165–178.
26 S. Zeng, P. Kar, U. K. Thakur and K. Shankar, *Nanotechnology*, 2018, **29**, 052001.
27 J. Zhang, J. H. Bang, C. Tang and P. V. Kamat, *ACS Nano*, 2009, **4**, 387–395.
28 M. Miyauchi, M. Takashio and H. Tobimatsu, *Langmuir*, 2004, **20**, 232–236.
29 J. Jiang, Y. Jia, Y. Wang, R. Chong, L. Xu and X. Liu, *Appl. Surf. Sci.*, 2019, **486**, 93–101.
30 M. Ahmadi, M. S. Dorraji, M. Rasoulifard and A. Amani-Ghadim, *Sep. Purif. Technol.*, 2019, **228**, 115771.
31 A. Kudo, R. Niishiro, A. Iwase and H. Kato, *Chem. Phys.*, 2007, **339**, 104–110.
32 A. B. Djurišić, Y. H. Leung and A. M. Ching Ng, *Mater. Horiz.*, 2014, **1**, 400–410.
33 K. Xie, N. Umezawa, Z. Ning, P. Reunchan, Y. Zhang and J. Ye, *Energy Environ. Sci.*, 2011, **4**, 4211–4219.
34 V. Jeyalakshmi, R. Mahalakshmy, K. R. Krishnamurthy and B. Viswanathan, *Catal. Today*, 2017, **300**, 152–159.
35 C. Tang, Y. Zhang and Z. Huang, *Renewable Sustainable Energy Rev.*, 2014, **30**, 195–216.
36 Y.-J. Gu, W. Wen, S. Zheng and J.-M. Wu, *Mater. Chem. Front.*, 2020, **4**, 2744–2753.
37 G. Zhang, W. Jiang, S. Hua, H. Zhao, L. Zhang and Z. Sun, *Nanoscale*, 2016, **8**, 16963–16968.
38 S. Bhardwaj and B. Pal, *Adv. Powder Technol.*, 2018, **29**, 2119–2128.
39 L. Mu, Y. Zhao, A. Li, S. Wang, Z. Wang, J. Yang, Y. Wang, T. Liu, R. Chen and J. Zhu, *Energy Environ. Sci.*, 2016, **9**, 2463–2469.
40 Y. Li, Y. Wang, W. Doherty, K. Xie and Y. Wu, *ACS Appl. Mater. Interfaces*, 2013, **5**, 8553–8562.
41 H. Tan, Z. Zhao, W.-b. Zhu, E. N. Coker, B. Li, M. Zheng, W. Yu, H. Fan and Z. Sun, *ACS Appl. Mater. Interfaces*, 2014, **6**, 19184–19190.
42 T. Kawabe, K. Tabata, E. Suzuki, Y. Yamaguchi and Y. Nagasawa, *J. Phys. Chem. B*, 2001, **105**, 4239–4244.
43 D. J. Seong, M. Jo, D. Lee and H. Hwang, *Electrochem. Solid-State Lett.*, 2007, **10**, H168–H170.
44 R. I. Eglitis and D. Vanderbilt, *Phys. Rev. B: Condens. Matter Mater. Phys.*, 2007, **76**, 155439.
45 R. Eglitis and D. Vanderbilt, *Phys. Rev. B: Condens. Matter Mater. Phys.*, 2008, **78**, 155420.
46 S. Woo, H. Jeong, S. A. Lee, H. Seo, M. Lacotte, A. David, H. Y. Kim, W. Prellier, Y. Kim and W. S. Choi, *Sci. Rep.*, 2015, **5**, 8822.
47 G. S. Foo, Z. D. Hood and Z. Wu, *ACS Catal.*, 2017, **8**, 555–565.
48 R. Li, H. Han, F. Zhang, D. Wang and C. Li, *Energy Environ. Sci.*, 2014, **7**, 1369–1376.
49 J. L. Giocondi and G. S. Rohrer, *J. Am. Ceram. Soc.*, 2003, **86**, 1182–1189.
50 T. Tachikawa and T. Majima, *Chem. Commun.*, 2012, **48**, 3300–3302.
51 T. W. Kim, Y. Ping, G. A. Galli and K.-S. Choi, *Nat. Commun.*, 2015, **6**, 8769.
52 H.-C. Chen, C.-W. Huang, J. C. Wu and S.-T. Lin, *J. Phys. Chem. C*, 2012, **116**, 7897–7903.
53 W. Wei, Y. Dai, M. Guo and B. Huang, *Appl. Surf. Sci.*, 2011, **257**, 6607–6611.
54 W. Wei, Y. Dai, K. Lai, M. Guo and B. Huang, *Chem. Phys. Lett.*, 2011, **510**, 104–108.

55 X. Wu, C. Wang, Y. Wei, J. Xiong, Y. Zhao, Z. Zhao, J. Liu and J. Li, *J. Catal.*, 2019, **377**, 309–321.
56 S. Xie, Y. Wang, Q. Zhang, W. Deng and Y. Wang, *ACS Catal.*, 2014, **4**, 3644–3653.
57 Y. Wei, X. Wu, Y. Zhao, L. Wang, Z. Zhao, X. Huang, J. Liu and J. Li, *Appl. Catal., B*, 2018, **236**, 445–457.
58 M. Tasbihi, F. Fresno, U. Simon, I. J. Villar-García, V. Pérez-Dieste, C. Escudero and V. A. de la Peña O'Shea, *Appl. Catal., B*, 2018, **239**, 68–76.
59 T. P. Xie, Y. Wang, C. L. Liu and L. J. Xu, *Materials*, 2018, **11**, 17.